Proceedings of the Thirty-second (2022) International Ocean and Polar Engineering Conference **www.isope.org**
Shanghai, China, June 5–10, 2022

ISBN 978-1-880653-81-4; ISSN 1098-6189

Numerical Investigation of Propeller-Rudder Interaction Based on Induct Factor Fitting Body Force Method

Mingzhe Wang, Jianhua Wang, Decheng Wan*
Computational Marine Hydrodynamics Lab (CMHL), School of Naval Architecture, Ocean and Civil Engineering,
Shanghai Jiao Tong University, Shanghai, China
* Corresponding Author

ABSTRACT

Using body force model based on blade element momentum theory instead of real propeller model can save considerable computational resources. However, due to the simplification of propeller geometry and the inapplicability of ideal fluid theory in viscosity solver, correction methods should be put forward to reduce the error. In this paper, the induct factor distribution is obtained by the projection model, and the numerical simulation of the propeller-rudder interaction between KP505 propeller and NACA0018 section rudder is carried out under five working conditions: J=0.1, 0.3, 0.5, 0.7 and 0.9. The results show that the body force model can capture the influence of non-uniform inflow, and the pressure distribution of rudder surface obtained by the two models are similar, which proves the capability of the body force model at different working conditions.

KEY WORDS: Blade element momentum theory; propeller-rudder interaction; body force; OpenFOAM; numerical simulation.

INTRODUCTION

Rudder is one of the most important appendages for ship maneuvering. In order to improve the rudder efficiency, the propeller is usually placed in front of the rudder to bring a higher inflow speed. This causes the inflow region of rudder being disturbed by the propeller. Propeller and rudder interference study needs a lot of experimental data support, which is a complex test. Computational Fluid Dynamics (CFD) is a developed method to research propeller-rudder interaction without expensive laboratorial equipment (Badoe et al., 2015). However, the time step and mesh size are limited due to the high rates rotating motion and complex geometric structure of the real propeller model, which makes direct numerical simulation very expensive. At the same time, it is generally not necessary to obtain all the details of the flow field in the long-time maneuverability test (Broglia et al., 2012), such as the interaction between the vortices separated by the rotating propeller and the aligned rudder. Therefore, body force model was proposed to replace the real propeller model, which as a source term directly involved in solving momentum equation.

As a body force model with moderate complexity and accuracy, blade element momentum theory has great application potential. In viscous flow CFD solver, there are two main problems to be solved in utilizing body force model based on traditional blade element momentum theory. One of the problem is that the airfoil data obtained based on wind tunnel tests are for the infinite airfoil with a given Reynolds number, and ignoring the three-dimensional effect. It means that direct calculation of propeller performance will lead to errors (Benini, 2004), which need to be corrected in practical application (MacNeill, 2017; Ortolani et al., 2018). Another problem is the way to calculate inflow velocity. If the foil performance was calculated by “inflow velocity” (far field velocity), the relationship between “local velocity” and “inflow velocity” must be established to get foil performance at specific working condition because the velocity field at propeller plane is disturbed by the propeller. This bridging function is assumed by induct factors. Traditionally, induct factors are derived iteratively based on ideal thruster theory, and does not consider the viscous effect and three-dimensional effect of the fluid. Thus, there will be an error between the result and the actual situation in RANS solver. These two constraints make the curve of blade element momentum theory’s error and advance ratio like a “V” shape. There will be an advance ratio $J0$ corresponding to the minimum error, and when the advance ratio is above or lower than J_0, the error will increase, which means this method can not meet propeller performance in different advance ratio conditions at the same time (Benini, 2004).

With the increasing accuracy of real propeller model, a direct projection model based on radial distribution of real propeller load is being widely used. The recent researches show that the body force model based on the radial distribution of real propeller load can be applied to some simple simulation (Villa et al., 2018; Bruzzone et al., 2014). However, this method uses two assumptions: The influence of flow field disturbance on propeller load is not considered, and the propeller load is uniformly distributed in circumferential direction, which means that this method cannot consider the influence of the

blocking effect of rudder on propeller performance.

In this paper, the blade element momentum theory is modified by fitting the induct factor, while the induct factor data are obtained using a projection model with the same radial load distribution as a real propeller. Besides, real propeller blade element performance instead of 2D airfoil performance is used, which has been introduced at the first part. The modified body force model is used to simulate propeller-rudder interaction with five different advance ratios. The second part of this paper reports the numerical background and induct factor fitting method. The third part presents the geometry and working conditions. Then the propeller-rudder interaction result is discussed. The final part displayed the summary of this paper.

NUMERICAL BACKGROUND

Governing Equations

In this paper, body force model and real propeller model are used to simulate propeller-rudder interaction. The CFD solvers used in the present work are pimpleFoam and pimpleDyMFoam in open source platform OpenFOAM. The solver allows users to easily modify the governing equations according to specific requirements. For incompressible viscous fluid, the N-S equation used to solve the flow field is in the following form:

$$\frac{\partial u_i}{\partial x_i} = 0 \tag{1}$$

$$\frac{\partial u_i}{\partial t} + \frac{\partial}{\partial x_j}(\rho u_i u_j) = -\frac{\partial p}{\partial x_i} + \frac{\partial}{\partial x_j}(\mu \frac{\partial u_i}{\partial x_j} - \rho \overline{u_i' u_j'}) + (f_\varepsilon)_i \tag{2}$$

where p is pressure, ρ is density, μ is viscosity coefficient, u_i is velocity component, $-\rho \overline{u_i' u_j'}$ is Reynolds stress. To close the equation, the Reynolds stress can be solved using turbulence model. As for the numerical simulation of propeller open water test, it has not been decided what is the most suitable turbulence model yet (Tu , 2019). In this paper, the k-ω SST model has been used. This turbulence model can activate different calculation methods of turbulence parameters based on the variation of distance from the wall surface. Detailed theories and equations can be obtained in relevant literature (Menter, 1994). $(f_\varepsilon)_i$ is the body force source term, which is calculated by the body force code provided separately(Churchfield and Lee, 2013). The switch between the two propeller models can be controlled by whether the source term is involved in the calculation. In order to compare the simulation results between the real propeller model and the body force model, unsteady simulation is adopted in this paper. Pimple method is used to decouple the velocity field from the pressure field. Here, the body force is solved by explicit method, which is, at each time step, the body force field of the previous time step is firstly used to solve the velocity field, and then the body force field is calculated by the velocity field of the current time step.

Blade Element Momentum Method

After solving the governing equation Eq. 1 and Eq. 2 each time, the blade element momentum theory code will run to solve the body force field. In this study, the effect of blade elements acts on points in the flow field, which is called the actuating points. The actuating points are arranged in radial and circumferential directions with equal spacing, and only one layer in the axial direction. This distribution itself has no effect of rotation. The rotational speed is only used to calculate the blade element hydrodynamic force. Since the hydrodynamic forces of each blade element do not affect each other, and the body force distribution is updated by the velocity field at each time step, unsteady problems and uneven flow problems can be dealt with. When calculating the hydrodynamic performance of each blade element, first, the velocity at each actuating points is obtained by interpolation of velocity field. Then according to Eqs. 3~14 and fig. 1, the interaction force between propeller model and fluid is obtained.

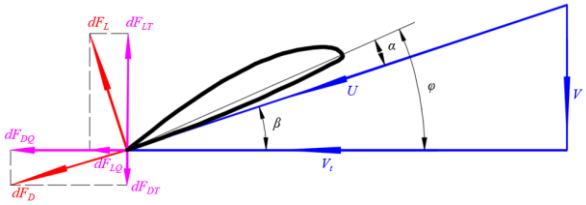

Fig. 1 Velocity and force relationship of blade element

$$V = \frac{V_x}{1+a} \tag{3}$$

$$V_t = \frac{V_\theta}{1+b} - 2\pi nr \tag{4}$$

$$U = \sqrt{(V_t + 2\pi nr)^2 + V^2} \tag{5}$$

$$\beta = \frac{V}{2\pi nr} \tag{6}$$

$$\alpha = \phi - \beta \tag{7}$$

$$dF_{\mathrm{L}} = \frac{1}{2} C_L U^2 c_r dr \tag{8}$$

$$dF_{\mathrm{D}} = \frac{1}{2} C_D U^2 c_r dr \tag{9}$$

$$dF_{\mathrm{T}} = dF_{\mathrm{L}} \cos\beta - dF_D \sin\beta \tag{10}$$

$$dF_{\mathrm{Q}} = (dF_{\mathrm{L}} \sin\beta + dF_D \cos\beta) r \tag{11}$$

$$F_{\mathrm{T}} = N \int_{R_{hub}}^{R_{tip}} dF_{\mathrm{T}} \tag{12}$$

$$F_{\mathrm{Q}} = N \int_{R_{hub}}^{R_{tip}} dF_{\mathrm{Q}} \tag{13}$$

$$\mathbf{f} = [\frac{NdF_x}{N_\theta}, \frac{NdF_y}{N_\theta}, \frac{NdF_z}{N_\theta}] \tag{14}$$

where a and b are axial induct factor and tangential induct factor, respectively. n is propeller rotation speed, r is the radial position of the blade element, V_x is local axial velocity, V_θ is local tangential velocity, V is axial inflow velocity, V_t is tangential inflow velocity, β is hydrodynamic pitch angle, Φ is blade element pitch angle, α is angle of attack, C_l and C_d are lift/drag force coefficient of blade element, c_r is the chord length at the corresponding radial position, dr is the span length of blade element, dF_L and dF_D are the lift/drag force of blade element, dF_T and dF_Q are the contribution of propeller thrust and torque of blade element, F_T and F_Q are the thrust and torque of propeller, R_{tip} is tip radius, R_{hub} is hub radius, N is the number of propeller blades, N_r is the radial number of blade elements, N_θ is the number of the actuating points in each circle, dF_x, dF_y, dF_z are the components of resultant force of blade element in global coordinates.

The force of blade element is projected in mesh as body force by Gaussian method. The body force of a grid is the accumulation of the influence of the surrounding actuating points. The weight of such influence is based on the distance between the grid point and the actuating point, and the weight calculation formula is Eq. 15. When the distance between the grid and the actuating point exceeds the preset

Gaussian projection distance, the grid is no longer affected by the actuating point. In this paper, the influence range of each actuating point ε is 0.01m. Eq. 16 is the accumulative formula for calculating the body force at each grid point.

$$\eta_\varepsilon(d)=\frac{1}{\varepsilon^3\pi^{3/2}}\exp[-(\frac{d}{\varepsilon})^2] \tag{15}$$

$$\mathbf{f}_\varepsilon=\sum_{i=1}^{N_{adp}}\mathbf{f}_i\frac{1}{\varepsilon^3\pi^{3/2}}\exp[-(\frac{d_i}{\varepsilon})^2] \tag{16}$$

where N_{adp} is the total number of actuating points, d_i is the distance between each cell's center and actuating points.

Blade Element Performance Data

The performance data of propeller blade element is the relationship between blade element lift/drag force coefficient and angle of attack, which should be stored in the file before body force model being used. Because the accuracy of blade element performance data directly affects the simulation results of the body force model, it is necessary to make it conform to the real blade element performance as much as possible. In this paper, the simulation results of real propeller openwater test are used to obtain the performance of blade element, and the data of blade element at each time step for body force model calculating is output by piecewise linear interpolation. The specific process is as follows: Firstly, the openwater test of the real propeller model is carried out, and the propeller is divided into different blade elements according to radial isometric distance. The blade elements at the same radial position have the same performance, that is, the propeller performance is circumferential average. The contribution of each blade element to torque dF_Q and thrust dFT is obtained by integrating surface pressure, as shown in Fig. 2. The lifting resistance coefficient of each blade element is calculated from Eqs. 17~22 while the angle of attack is calculated from Eqs. 5~7, Where V is "inflow velocity". The angle of attack, lift coefficient and drag coefficient are stored as vectors in corresponding files for interpolation reading by body force program. In the blade element calculation program, the lifting drag coefficients Cl and Cd in Eqs. 8~9 are obtained by piecewise linear interpolation of the blade element's α, the stored blade element's angle of attack vector $\boldsymbol{\alpha}$ and lift/drag force coefficient vector $\mathbf{C_l}$ and $\mathbf{C_d}$. This interpolation scheme can minimize the error in data processing as Eqs. 21~ 22.

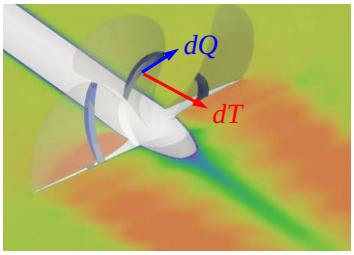

Fig. 2 Propeller blade element

$$dF_L=\frac{dQ/r\cos\beta+dT/\sin\beta}{\cos\beta/\sin\beta+\sin\beta/\cos\beta} \tag{17}$$

$$dF_D=\frac{dQ/r\sin\beta-dT/\cos\beta}{\cos\beta/\sin\beta+\sin\beta/\cos\beta} \tag{18}$$

$$\mathbf{C_L}(r)=\frac{2dF_L}{U^2c_r dr} \tag{19}$$

$$\mathbf{C_D}(r)=\frac{2dF_D}{U^2c_r dr} \tag{20}$$

$$\begin{aligned}C_l&=f_1(\alpha,r)\\&=\mathbf{C_{l}}_{i-1}(r)\times\frac{\alpha-\boldsymbol{\alpha}(r)_i}{\boldsymbol{\alpha}(r)_{i-1}-\boldsymbol{\alpha}(r)_i}+\mathbf{C_{l}}_{i}(r)\times\frac{\alpha-\boldsymbol{\alpha}(r)_{i-1}}{\boldsymbol{\alpha}(r)_i-\boldsymbol{\alpha}(r)_{i-1}},\end{aligned} \tag{21}$$

$$\alpha\in[\boldsymbol{\alpha}(r)_{i-1},\boldsymbol{\alpha}(r)_i]$$

$$\begin{aligned}C_d&=f_1(\alpha,r)\\&=\mathbf{C_{d}}_{i-1}(r)\times\frac{\alpha-\boldsymbol{\alpha}(r)_i}{\boldsymbol{\alpha}(r)_{i-1}-\boldsymbol{\alpha}(r)_i}+\mathbf{C_{d}}_{i}(r)\times\frac{\alpha-\boldsymbol{\alpha}(r)_{i-1}}{\boldsymbol{\alpha}(r)_i-\boldsymbol{\alpha}(r)_{i-1}},\end{aligned} \tag{22}$$

$$\alpha\in[\boldsymbol{\alpha}(r)_{i-1},\boldsymbol{\alpha}(r)_i]$$

Induct factor fitting method

Induct factor *a* is the relationship between inflow velocity and local velocity as shown in Fig. 3. Traditional blade element momentum theory for solving the induct factor is based on the ideal fluid theory (Benini, 2004; Winarto, 2004), which is not suitable for body force model couple with viscosity solver. Therefore, a new method is needed to study the relationship between local velocity and inflow velocity. In order to obtain this relationship, a stable propeller openwater test field should be obtained first, and the corresponding local velocity of each blade element should be read from it. The following methods are adopted in this paper: based on the performance data of blade element obtained above and from Eqs. 16~20, the lift/drag force distribution of blade element at a certain inflow velocity can be obtained, and the body force distribution can be obtained from Eq. 16. The body force distribution is simulated by open water test under corresponding working conditions without iterating with velocity field. In this condition, the body force load distribution accords with the radial distribution of real propeller load, which works like the projection model. The local velocity of each blade element was obtained by interpolating from the stable velocity field at the position of the blade element, as shown in Fig. 4.

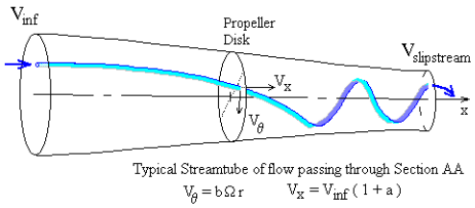

Fig. 3 Ideal propeller theory (Winarto, 2004)

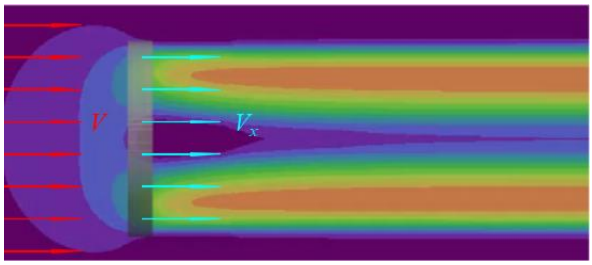

Fig. 4 Openwater flow field based on real propeller load

The local velocity corresponding to the blade element in each radial position is the circumferential mean of velocity at the actuation points for a cycle. The corresponding relationship between the local velocity at each radial position and the inflow velocity can be established, and the induct factor corresponding to different local velocities can be obtained. Here is the specific equation for fitting the induct factor: First, considering that the inflow velocity and local velocity satisfies a linear

relationship:

$$V^{'} = A(R^{'})V_x^{'} + B(R^{'}) \tag{23}$$

where $A(R^{'})$, $B(R^{'})$ are the coefficients to be fitted, and $V^{'}$, $V_x^{'}$, $R^{'}$ are the dimensionless inflow velocity, local axial velocity and radial position respectively:

$$V^{'} = \frac{V}{nD} \tag{24}$$

$$V_x^{'} = \frac{V_x}{nD} \tag{25}$$

$$R^{'} = \frac{R}{R_{tip}} \tag{26}$$

D is the diameter of propeller. The fitting formula of induct factor distribution can be obtained by combining Eq. 3 and Eq. 23:

$$a = \frac{V_x^{'}}{A(R^{'})V_x^{'} + B(R^{'})} - 1 \tag{27}$$

By changing the advance ratio, the relation of $R^{'}$ and $A(R^{'})$, $B(R^{'})$ can be acuqired. Using quintic polynomial fitting, the following equation can be obtained:

$$\begin{bmatrix} A(R^{'}) \\ B(R^{'}) \end{bmatrix} = \begin{bmatrix} J_{11}R^{'5} + J_{12}R^{'4} + J_{13}R^{'3} + J_{14}R^{'2} + J_{15}R^{'} + J_{16} \\ J_{21}R^{'5} + J_{22}R^{'4} + J_{23}R^{'3} + J_{24}R^{'2} + J_{25}R^{'} + J_{26} \end{bmatrix} \tag{28}$$

The coefficient matrix format and calculation method of tangential induct factor *b* are the same as that of axial induct factor. By storing coefficient matrix **J**, the blade element momentum theory program can calculate $A(R^{'})$, $B(R^{'})$ at each radial position. In the process of each iteration, the induct factor at each radial position will be obtained from the corresponding $A(R^{'})$, $B(R^{'})$ and local velocity V_x. In other words, this method establishes the corresponding relationship between the local velocity of the blade element and its load under viscous flow conditions. In this way, the present approach can avoid the limitation of the ideal fluid theory hypothesis.

GEOMETRY AND MESH

The geometry of propeller-rudder interaction study is the KP505 propeller model and the rudder model with NACA0018 section, which is from the benchmark Case3.2 of SIMMAN2020 for KCS ship model.

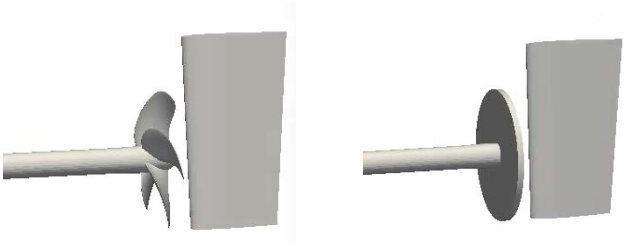

(a) real propeller model (b) body force model

Fig. 5 Model arrangement

The propeller diameter D is 0.2085m and the rudder span is 0.28m. In the propeller-rudder interaction, the propeller was set in front of the rudder while the gap between two components X/D is 0.19. The distribution range of body force and propeller-rudder arrangement are shown in Fig. 5. In the present study, this configuration has been tested in five different inflow conditions, as the corresponding advance radios were *J*=0.4, 0.5, 0.6, 0.7, 0.8, 0.9. The angle of attack of rudder was set to zero, which means complex separation flow was not considered in this paper.

The computational domain was set to a box, and the inlet and outlet were far enough to prevent unexpected disturbance as reported in Fig. 6. Wall condition was applied to propeller and rudder boundaries. The rest boundary are all far field condition. Propeller rotating was realized though sliding mesh. After the refinement around the propeller and rudder surface, the mesh number reached 1.71 million for real propeller model and 0.89 million for body force propeller model as shown in Fig. 7. The mesh independence research and timestep independence research were performed in previous work (Ren et al., 2020). The time step is set to be 0.001s for body force model and 0.00046s for real propeller model. What's more, to get the induct factor distribution based on real propeller load, five openwater tests with the same mesh and numerical scheme without considering rudder were processed. The advance ratio of openwater tests were set to be *J*=0.2, 0.4, 0.6, 0.8, 0.9, and these tests no longer listed separately.

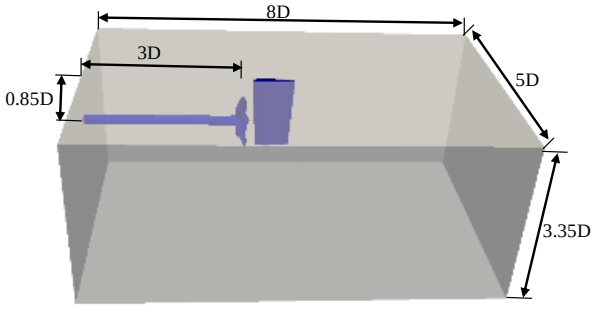

(a) real propeller model

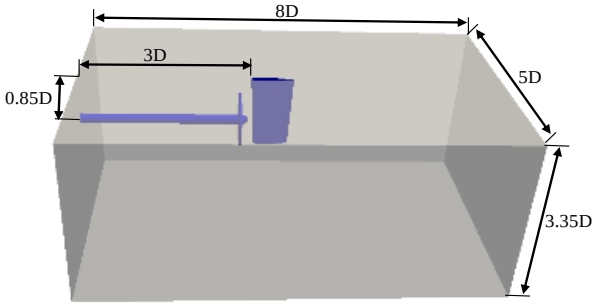

(b) body force model

Fig. 6 Computational domain

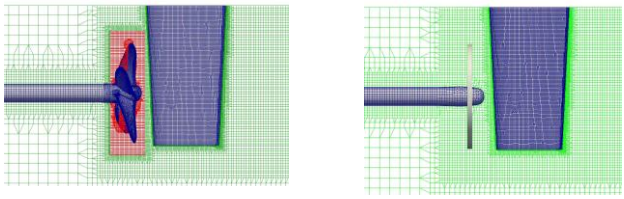

(a) real propeller model (b) body force model

Fig. 7 Mesh distribution

RESULTS AND DISCUSSIONS

Fig. 8 shows the fitting results of Eq. 27 at different radial positions on the axial induct factor distribution of the propeller. "CFD" represents the relationship between the axial induct factor obtained based on the real propeller load distribution and the dimensionless local velocity. "Fitting" represents the fitting result of Eq. 27. The two groups of data points in the figure are consistent, indicating that Eq. 27 can fit the

general law of axial induct factor and local velocity. Although When R'=0.2, the fitting effect is poor, that's because it is located on the surface of the hub and the influence of the propeller shaft is not considered in the numerical calculation. At the same time, for the data point of J=0.2 (for example, $V_x{}'$=0.37, a=0.85 when R' =0.28), the local velocity no longer meets the linear relationship with the flow at infinity, and the axial induction factor also deviates greatly from the fitting curve. In the normal working range of propeller (J=0.4~0.8), the fitting effect of Eq. 27 is good. Fig. 9 shows the fitting effect of tangential induct factor. Different from axial induct factor, there is a high consistency between tangential induct factor and fitting result. Data in figure 8 and figure 9 shows that the the linear hypothesis in Eq. 23 of inflow velocity and local velocity is applicable, at the same time can be found in advance and speed increases. Besides, as the local axial velocity and local tangential velocity increases, the axial induced factors and tangential induced factor respectively decrease(absolute value). This is because in the range of propeller design working conditions, the increase of advance velocity and rotate speed will lead to the decrease and increase of propeller load respectively, and the advance velocity and rotate speed play a controlling role on the local axial/ tangential velocity.

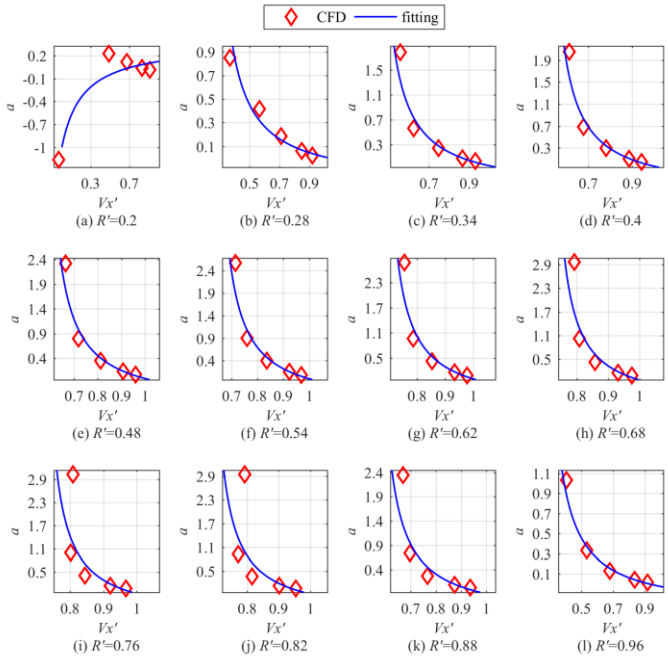

Fig. 8 Axial induct factor fitting

Table 1 shows the propeller open water test data obtained by fitting induct factor method against with real propeller model. Because the fitting error of fitting curve to different data points is not the same, the error characteristics are not completely the same for every working conditions. The open water test results of body force model are very good at medium advance rate (J=0.4~0.8), while the error increases when J=0.2 and J=0.9.

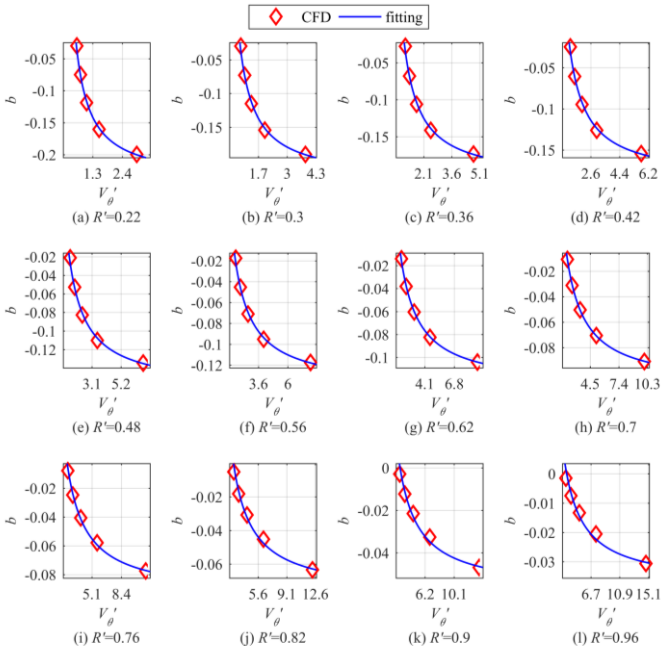

Fig. 9 Tangential induction factor fitting

The axial induct factor has a large fitting error as shown in Fig. 8. For J=0.9, although the fitting curve shows good agreement with data, the fitting error still has a large influence to openwater test result due to the small value of propeller load in this working condition. This condition depends on the fitting form as Eq. 27. The maximum thrust error and torque error of each working condition is not more than 13%, and most of them are within 4%. It is proved that the body force model can be used to simulate the propeller-rudder interaction.

Table 1. Body force model open water data

J	0.2	0.4	0.6	0.8	0.9
Body force KT	0.396	0.334	0.241	0.128	0.065
Real model KT	0.429	0.336	0.235	0.129	0.074
Error KT	7.73%	0.62%	2.56%	0.78%	12.42%
Body force KQ	0.0564	0.0484	0.0363	0.0211	0.0120
Real model KQ	0.0604	0.0482	0.0351	0.0211	0.0136
Error KQ	6.56%	0.37%	3.55%	0.19%	11.39%

Because of block effect, propeller before the rudder will meet a lower inflow velocity compared with openwater test near the rudder surface. This situation will cause uneven inflow, and finally affects load on propeller. Real propeller model and body force model will response to this effect as reported in Fig. 10, where the body force distribution and propeller pressure distribution on surface of each cases are listed, which shows the consistent behavior of propeller and body force model under blocking effect. Not surprisingly, for the body force propeller case, the body force distribution is not even, and high load zone focus on the mid vertical plane (near the rudder). For the real propeller case, blades which move close to the rudder surface get more high pressure area than other blades. This feature won't be captured by projection model, which don't iterate propeller load during the simulation processing.

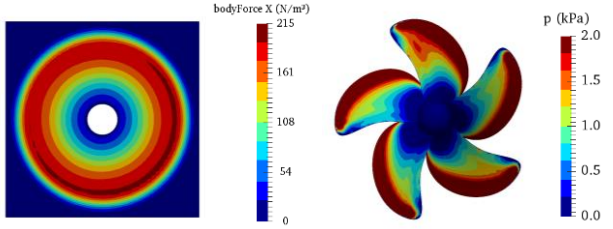

(a) body force distribution(J=0.1) (b) propeller pressure distribution(J=0.1)

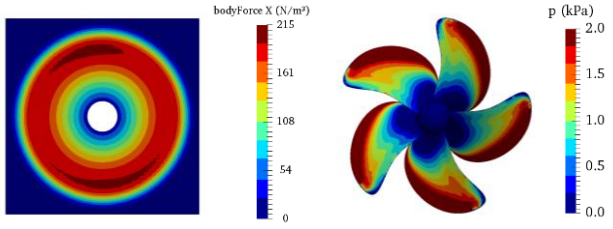

(c) body force distribution(J=0.3) (d) propeller pressure distribution(J=0.3)

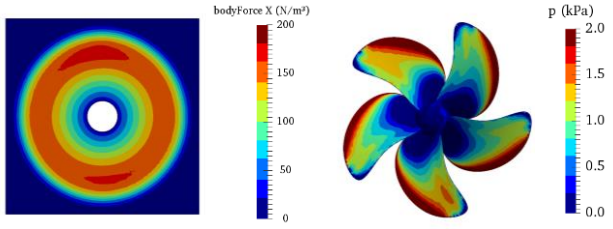

(e) body force distribution(J=0.5) (f) propeller pressure distribution(J=0.5)

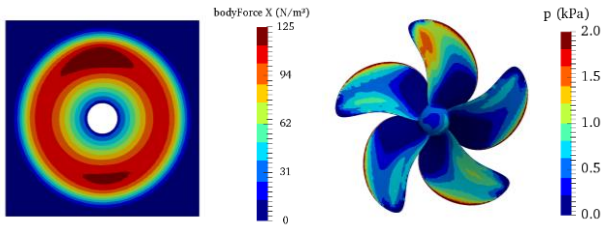

(g) body force distribution(J=0.7) (h) propeller pressure distribution(J=0.7)

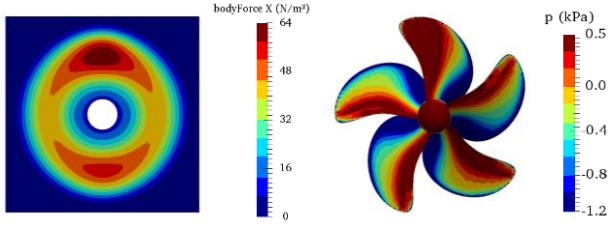

(i) body force distribution(J=0.9) (j) propeller pressure distribution(J=0.9)

Fig. 10 Propeller load distribution for both model

In order to verify the accuracy of induct factor fitting method in the problem of propeller-rudder interaction, pressure distribution on rudder surface was chosen to be analyzed. The pressure distribution counter for both sides in each case is shown in Fig. 11. The high pressure zone and low pressure zone on leading edge is caused by propeller rotating effect, which was captured by body force model. The pressure distribution is basically the same for body force model case and real propeller model case, except for some local details. To show more details of pressure field, pressure distribution on three slices of rudder surface is selected. The position of these slices is shown in Fig. 12, which located in the center of high pressure area and low pressure area, and the position of propeller axis, respectively. The slice vertical coordinate are -0.06m, 0m and 0.06m.

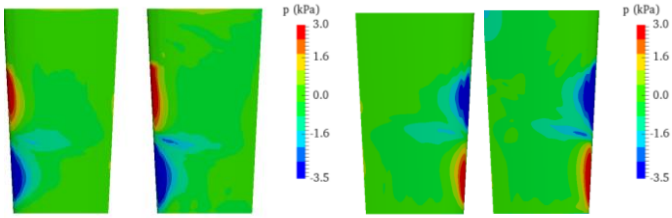

(a) rudder starboard pressure distribution(J=0.1) (b) rudder port pressure distribution(J=0.1)

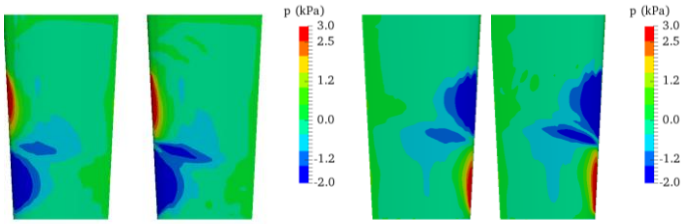

(c) rudder starboard pressure distribution(J=0.3) (d) rudder port pressure distribution(J=0.3)

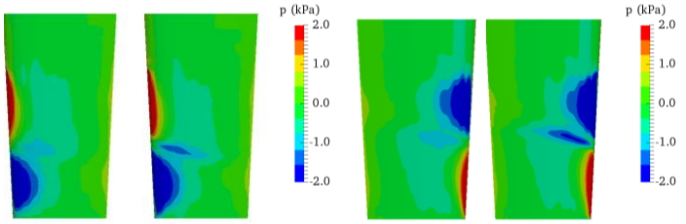

(e) rudder starboard pressure distribution(J=0.5) (f) rudder port pressure distribution(J=0.5)

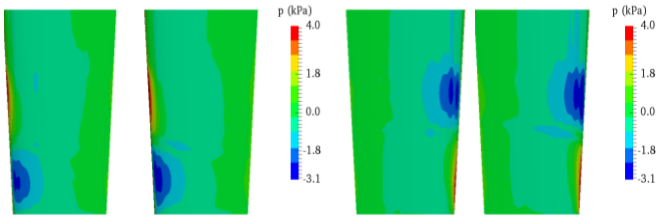

(g) rudder starboard pressure distribution(J=0.7) (h) rudder port pressure distribution(J=0.7)

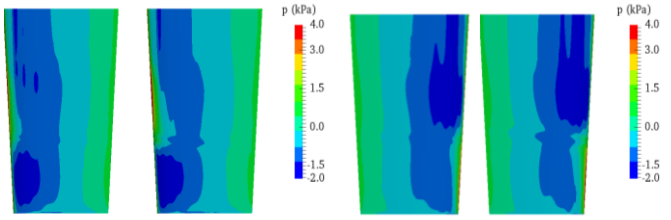

(i) rudder starboard pressure distribution(J=0.9) (j) rudder port pressure distribution(J=0.9s)

Fig. 11 Pressure distribution on rudder surface (left: Body force model; right: Real propeller model)

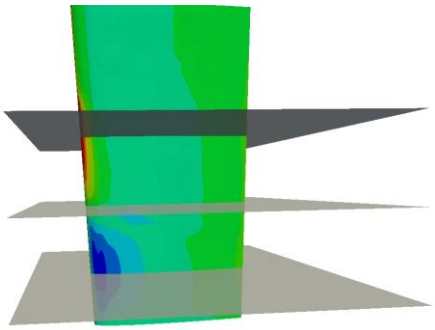

Fig. 12 Slice positions on the rudder

In Fig. 13, the x-axis represents the dimensionless chordal coordinates, where c_{slice} represents the chord length of the corresponding rudder section. x/c_{slice} = 0 means the leading edge of the rudder. It can be seen from Fig 13 that under the condition of five kinds of advance ratio, the rudder surface pressure under two propeller model action at the position of z= ±0.06m much well (Fig. 13 (b), (c), (e), (f), (h), (i), (k), (l), (n), (o)). For the data at section z=0 (Fig. 13 (a), (d), (g) , (j) , (m)), when x/c_{slice} >0.2, the two groups of data are in good agreement. When x/c_{slice} <0.2, the pressure near the leading edge of the rudder surface under the action of real propeller is lower (blue lines). This feature can also be observed in Fig. 12, that under the action of the real propeller model, the low pressure area on the rudder surface near the propeller hub is larger than that under the action of the body force model. This is caused by the local vorticity fluctuation of the real propeller. Taking J=0.7 as an example, Fig. 14 shows the vortex structure under the action of the body force model and the real propeller model.

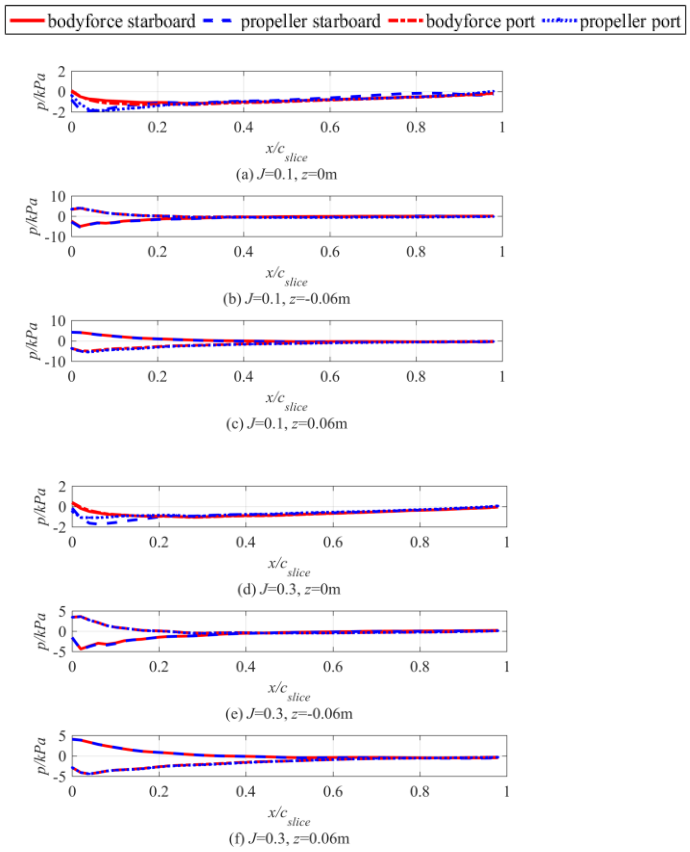

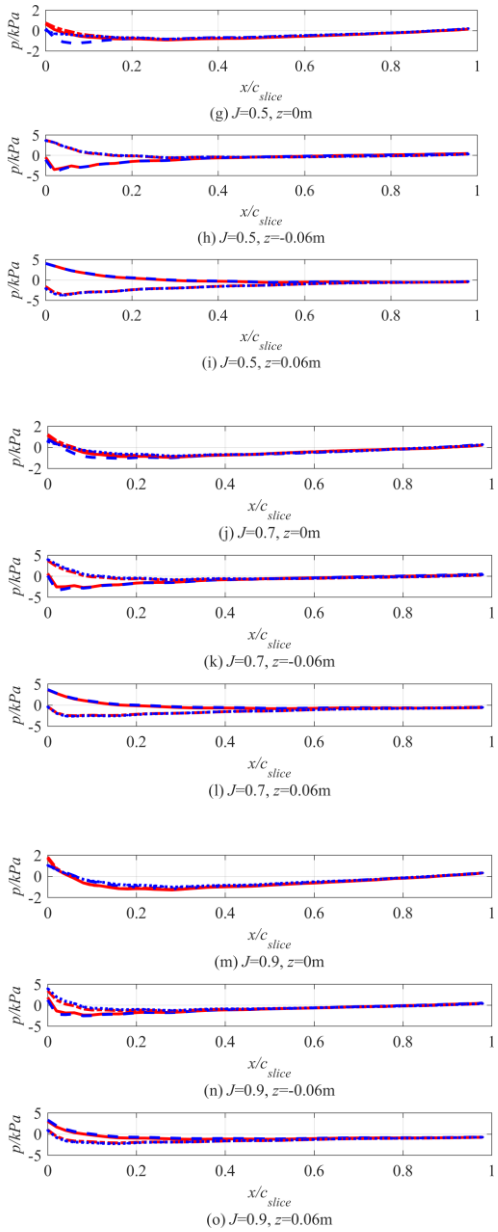

Fig. 13 Pressure distribution on different slices

Due to the refinement length of mesh is not too long, the vortex structure dissipates quickly after passing through the rudder, but abundant details of the flow field near the rudder surface have been left for the study anyway. In order to show the vortex structure near the rudder surface, part of the tip vortex of real propeller model around the outer side was cutted. For the body force model, the tip vortex are distributed in circumferential uniform circles, and only exist near the propeller plane due to the unsteady influence of the blade rotation is ignored in the body force model. In addition, since the hub rotation is not considered, the rotation effect of blade root is weak, and the vortex structure is smooth, resulting in a relatively stable flow field near the rudder surface under the action of body force model. The flow field near the surface of the rudder under the action of real propeller model is not only producing more intense hub vortices, but also affected by the vortex leakaged from the following edge of the propeller, and both of them make a contribution to the flow field disturbance near the hub,

causing a complicated vortex structure near this region. Finally the high rates vortices cause a lower pressure area, resulting in the difference of rudder pressure distribution between real propeller model and body force model. Although there is a difference in the details of the local flow field, it does not have a great influence on the hydrodynamic performance of the rudder based on the surface pressure integral.

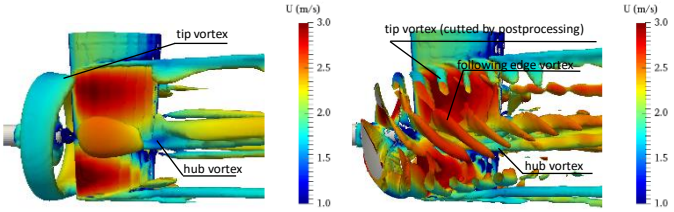

(a) body force vortex structure (b) real propeller vortex structure

Fig. 14 Vortical structure around the rudder (J=0.7)

CONCLUSIONS

In this paper, the induct factor distribution corresponding to the real propeller load is obtained by using the projection model, and the application of the theoretical volume force model of the blade element momentum in the viscosity solver is extended by using the three-dimensional blade element information of the propeller, and the numerical simulation of the propeller and rudder interaction between KP505 propeller and NACA0018 rudder under five advance speed conditions is carried out. The simulation results show that the induct factor fitting method body force model can not only capture the nonuniformity of the propeller load distribution caused by the blocking effect of the rudder, but also ensure the consistency of the pressure distribution of the rudder surface with the real propeller model at different working conditions. Because the vortical structure generated by the real propeller model is more complex, the pressure distribution of the rudder surface under the action of the two models show little discrepancy, but it does not affect too much on the application of the body force model. In the future, more accurate fitting forms will be studied so that the body force model can achieve higher accuracy for more working conditions.

ACKNOWLEDGEMENTS

This work is supported by the National Key Research and Development Program of China (2019YFB1704205), the National Natural Science Foundation of China (51809169), to which the authors are most grateful.

REFERENCES

Badoe, C, E, Phillips, A, B, and Turnock, S, R (2015). "Influence of drift angle on the computation of hull–propeller–rudder interaction," *Ocean Engineering*, 103, 64-77.

Benini, E (2004). "Significance of blade element theory in performance prediction of marine propellers," *Ocean Engineering*, 31, 957-974.

Broglia, R, Dubbioso, G, Durante, D (2012). "Simulation of turning circle by CFD: Analysis of different propeller models and their effect on manoeuvring prediction," *Applied Ocean Research*, 39, 1-10.

Bruzzone, D, Gaggero, S, and Bonvino, C, P (2014). "Rudder-propeller interaction: Analysis of different approximation techniques," *Proceedings of the 11th International Conference on Hydrodynamics*, Singapore, ICHD, 19-24.

Churchfield, M, Lee, S (2013). NWTC design codes (SOWFA) http://wind.nrel.gov/designcodes/simulators/SOWFA.

MacNeill, R, and Verstraete, D (2017). "Blade element momentum theory extended to model low Reynolds number propeller performance," *The Aeronautical Journal*, 121, 835-857.

Menter, F, R (1994). "Two-equation eddy-viscosity turbulence models for engineering applications," *AIAA Journal*, 32(8), 1598-1605

Ortolani, F, Dubbioso, G, and Muscari, R (2018). "Experimental and Numerical Investigation of Propeller Loads in Off-Design Conditions," *Journal of Marine Science and Engineering*, 6, 45-68

Ren, Z, Wang, J, and Wan, D (2020). "Numerical investigation of propeller-rudder interaction based on body force approach," *Proc 30th Int Offshore and Polar Eng Conf*, Shanghai, ISOPE, 1098-6189.

Tu, T, N (2019). "Numerical simulation of propeller open water characteristics using RANSE method," *Alexandria Engineering Journal*, 58(2), 531-537.

Villa, D, Viviani, M, and Tani, G (2018). "Numerical Evaluation of Rudder Performance Behind a Propeller in Bollard Pull Condition," *Journal of Marine Science and Application*, 17(2), 153-164.

Winarto, H (2004). "BEMT Algorithm for the Prediction of the Performance of Arbitrary Propellers," Melbourne: The Sir lawrence Wackett Centre for Aerospace Design Technology, Royal Melbourne Institute of Technology.